Anti-precipitation molecular metal chalcogenide complexes modification for efficient direct alkaline seawater splitting at the large current density

Liang Zhao [a], Shuanglong Zhou [a], Zheng Lv [a], Wenxia Xu [a], Jiaxin Liu [a], Ziyi Liu [a], Qi Zhang [a], Jianping Lai [a,*], Lei Wang [a,b,**]

[a] *Key Laboratory Base of Eco-Chemical Engineering, Ministry of Education, International Science and Technology Cooperation Base of Eco-chemical Engineering and Green Manufacturing, College of Chemistry and Molecular Engineering, Qingdao University of Science and Technology, Qingdao 266042, PR China*
[b] *Shandong Engineering Research Center for Marine Environment Corrosion and Safety Protection, College of Environment and Safety Engineering, Qingdao University of Science and Technology, Qingdao 266042, PR China*

ARTICLE INFO

ABSTRACT

Hydrogen production from direct alkaline seawater electrolysis at large current density is a key technology for marine energy projects. However, catalyst poisoning due to insoluble precipitation is a key issue that should be addressed. In this work, we used Pt/CNT electrocatalysts modified with molecular metal chalcogenide complexes. During the direct electrolysis of alkaline seawater, the modified Pt/CNT electrocatalyst can effectively reduce the formation of insoluble precipitates on the cathode surface, which is conducive to the stable operation of the hydrogen evolution reaction. Theoretical simulations and *in situ* experiments both demonstrate that the modified Pt/CNT was affected by the coordination to form coordination compounds, which effectively prevented the formation of insoluble precipitates. The alkaline anion exchange membrane (AEM) electrolyzer with a modified Pt/CNT electrocatalyst exhibited an industrially required current density of 1.0 A cm^{-2} at 2.0 V and 60 °C, achieving long-term stability in excess of 600 h.

1. Introduction

The excessive use of fossil fuels has caused more and more serious pollution to the environment [1–5]. Therefore, there is an urgent need to develop sustainable clean energy. High-purity hydrogen (H$_2$) produced by hydro electrolysis has the characteristics of high energy density, non-poisoning, and zero pollution [6–9]. It is a new energy source with zero carbon emission, and is considered an ideal fuel to deal with environmental and energy problems [10–16]. So far, many high-purity freshwater alkaline electrolytic cells have been developed for small-scale hydrogen production. However, industrial electrolysis of freshwater is highly dependent on site-specific water resources and may be limited in some areas [17–22]. Seawater accounts for more than 97% of the Earth's total water, and abundant seawater resources are needed to produce hydrogen on a large scale and sustainably [23–26]. However, direct seawater electrolysis has been less studied due to the complexity of natural seawater [27–29]. Current research, the integration of *in situ* water purification processes based on self-driven phase transition mechanisms into seawater electrolysis solves the problem of side reactions.[30] However, this study cannot be separated from a self-breathable waterproof membrane. Recent literature has reported that local alkalinity generated *in situ* avoids the formation of precipitates on the electrode [31]. The above study is about the direct electrolysis of neutral seawater [32–35]. Direct electrolysis of alkaline seawater at the large current density is now more attractive, not only to match industrial production but also to inhibit the oxidation of chlorine[36–40]. However, this process has not yet been implemented. This is because during the large current density of the cathode hydrogen evolution, a large amount of cations (Mg^{2+}, Ca^{2+}) are adsorbed on the cathode surface by electrostatic effects, producing more insoluble precipitates on the catalyst surface [41–46]. Therefore, there is a need to develop an electrocatalyst with high activity, stability and corrosion resistance to improve the stability of hydrogen production from direct electrolysis of seawater [46–50].

---

* Corresponding author.
** Corresponding author at: Key Laboratory Base of Eco-Chemical Engineering, Ministry of Education, International Science and Technology Cooperation Base of Eco-chemical Engineering and Green Manufacturing, College of Chemistry and Molecular Engineering, Qingdao University of Science and Technology, Qingdao 266042, PR China.

E-mail addresses: jplai@qust.edu.cn (J. Lai), inorchemwl@126.com (L. Wang).

Herein, we synthesized a class of anti-precipitation HER electrocatalysts with modified Pt/CNT electrocatalysts using molecular metal chalcogenide complexes. The modified Pt/CNT electrocatalyst can effectively block the contact of Mg^{2+} and Ca^{2+} with the active site in seawater and improve the stability of the electrocatalyst. By optimizing the amount of $(N_2H_5)_4Mo_2S_6$ solution, the optimized Pt/CNT-$_{200}(N_2H_5)_4Mo_2S_6$ achieves efficient alkaline seawater hydrogen evolution with excellent electrocatalytic performance. In the stability test, the current density of the modified Pt/CNT electrocatalyst remained almost unchanged and maintained good stability, while the unmodified Pt/CNT electrocatalyst was affected by the deposition and shedding of insoluble precipitates such as $Mg(OH)_2$ and $Ca(OH)_2$, and the current density would have large fluctuations. The catalytic mechanism of the catalyst was explained by *in situ* Fourier transform infrared spectroscopy (FTIR), *in situ* Raman spectroscopy, and density functional theory (DFT) calculations: the modified Pt/CNT electrocatalyst not only reduces the Pt-H bonding capacity and promotes the adsorption of H* , but also promotes dissociation of H_2O. During the direct electrolysis of alkaline seawater, ligand compounds are formed by the effect of coordination, which effectively prevents the formation of insoluble precipitates and enables the electrocatalyst to operate stably during the electrolysis of alkaline seawater. We further assembled an anion exchange membrane water electrolysis cell (AEM) using this catalyst as the anode and cathode. AEM achieved an industrial current density of 1 A cm^{-2} at a low battery voltage of 2.0 V, without the need for iR correction. Its durability exceeded 600 h and its performance was superior to commercial Pt/C and RuO_2.

2. Experimental section

2.1. Materials synthesis

2.1.1. Materials

Platinum(II)2,4-pentanedionate (Pt(acac)$_2$, Macklin, 97%), molybdenum powder (Mo, Macklin , >99.0%), tin powder (Sn, Macklin, 99.99%), sublimated sulfur (S, Aladdin, 99.99%), selenium Powder (Se, Aladdin, 99.99%), tellurium powder (Te, Aladdin, 99.99%), sodium hydroxide (NaOH, 96%), hydrazine hydrate ($N_2H_4 \cdot H_2O$, 80%).

2.1.2. Preparation of Pt/CNT

Pt(acac)$_2$ (10 mg) and CNT (10 mg) were mixed evenly and placed into a quartz vial, and argon was injected for 5 min. The mouth of the bottle was sealed with tin foil and placed in a microwave oven for 120 s reaction. Subsequently, the quartz vial was allowed to cool naturally to room temperature. Finally, the vials were washed twice with deionized water and twice with ethanol and collected by centrifugation.

2.1.3. Synthesis of molecular metal chalcogenide complexes

S-N_2H_4. S powder is dissolved in 80% hydrazine hydrate to obtain 1 M S-N_2H_4 solution.

Se-N_2H_4. Se powder is dissolved in 80% hydrazine hydrate to obtain 1 M Se-N_2H_4 solution.

Te-N_2H_4. Te powder is dissolved in 80% hydrazine hydrate to obtain 1 M Te-N_2H_4 solution.

$(N_2H_5)_4Mo_2S_6$. Mo powder (9.6 mg, 0.1 mmol) was dissolved in a mixture of 3 mL 1 M S-N_2H_4 solution and 1 mL 80% hydrazine hydrate and stirred at 130 °C for 72 h to form an transparent solution.

$(N_2H_5)_4Sn_2S_6$. Sn powder (11.8 mg, 0.1 mmol) was dissolved in a mixture of 3 mL 1 M S-N_2H_4 solution and 1 mL 80% hydrazine hydrate and stirred at 130 °C for 72 h to form an transparent solution.

$(N_2H_5)_4Mo_2Se_6$. Mo powder (9.6 mg, 0.1 mmol) was dissolved in a mixture of 3 mL 1 M Se-N_2H_4 solution and 1 mL 80% hydrazine hydrate and stirred at 130 °C for 72 h to form an transparent solution.

$(N_2H_5)_4Sn_2Se_6$. Sn powder (11.8 mg, 0.1 mmol) was dissolved in a mixture of 3 mL 1 M Se-N_2H_4 solution and 1 mL 80% hydrazine hydrate and stirred at 130 °C for 72 h to form an transparent solution.

$(N_2H_5)_4Mo_2Te_6$. Mo powder (9.6 mg, 0.1 mmol) was dissolved in a mixture of 3 mL 1 M Te-N_2H_4 solution and 1 mL 80% hydrazine hydrate and stirred at 130 °C for 72 h to form an transparent solution.

$(N_2H_5)_4Sn_2Te_6$. Sn powder (11.8 mg, 0.1 mmol) was dissolved in a mixture of 3 mL 1 M Te-N_2H_4 solution and 1 mL 80% hydrazine hydrate and stirred at 130 °C for 72 h to form an transparent solution.

2.1.4. Combinations of Pt/CNT complexes with metallic chalcogenides (Pt/CNT-$_x(N_2H_5)_4Mo_2S_6$)

At room temperature, appropriate amount of supernatant after oil bath was mixed with Pt/CNT (1 mg), stirred for 4 h, vacuumized and filtered for many times, and then freezed-dried. Obtain Pt/CNT-$_x(N_2H_5)_4Mo_2S_6$ powder (x represents the amount of solution added, μL).

2.2. Materials characterizations

To study the morphology and structure of the catalyst, a scanning electron microscope (SEM) was tested on Hitachi S-4800 instrument. The morphologies of the samples were characterized by transmission electron microscopy (TEM) and high-resolution TEM (HR-TEM) on a JEM-2100UHR at an accelerating voltage of 200 KV. X-ray diffraction (XRD) analysis at a scanning rate of 1°min^{-1} in the 2θ ranges from 5° to 90° was used to examine the composition of the as-synthesized samples on X'Pert PRO MPD diffractometer (Netherlands PANalytical) operating at 40 KV and 40 mA with Cu Kα radiation. X-ray photoelectron spectra (XPS) were collected with a VG ESCALABMK II spectrometer. The content of elements is determined by inductively coupled plasma atomic emission spectrometer (ICP-AES, Varian 710-ES). All the electrochemical performances of the as-synthesized samples were carried out on an electrochemical station (CHI 660E).

2.3. Electrochemical characterization for HER

On CHI660 electrochemical workstation (Shanghai Chenhua Instrument Corporation, China), the electrochemical measurements were carried out in a conventional three-electrode tank with platinum electrode as the opposite electrode and saturated calomel electrode as the reference electrode. All electrochemical measurements were converted to RHE. The potential conversion formula is E (RHE) = E (SCE) + 0.244 V + 0.0592 × pH. Glassy carbon electrode (GCE, diameter 3 mm, area 0.07065 cm^2). The different catalysts were dispersed in 1.0 mL anhydrous ethanol and 50 μL Nafion solution (5.0 wt%) and ultrasonic for 1 h to form a homogeneous catalyst ink with a concentration of 1 mg/mL. Then 10 μL electrocatalyst was dropped on the GCE surface for further electrochemical testing. HER measurements were made in a mixed solution of alkaline seawater. The polarization curves were collected at a scan rate of 5 mV s^{-1} with 95% iR correction. Before collecting, several fast cyclic voltammograms (CVs, 500 mV s^{-1}) were taken to clean and stabilize the electrocatalyst surface till steady-state was received. The Nyquist plots were performed at frequencies ranging from 100,000–0.1 Hz with an amplitude voltage of 5 mV.

2.4. Measurement of ECSA

The ECSA of the catalyst is calculated using Cu under-potential deposition (Cu-UPD) method. The ECSA of catalysts were calculated by integrating the charge associated with oxidation of Cu (on the surface of catalyst by Cu-UPD) in electrolyte containing 50 mM CuSO$_4$ and 0.5 M H$_2$SO$_4$, by assuming a charge of 420 μC cm^{-2}. The ECSA can be calibrated as:

$$ECSA(cm^2_{metal}/g_{metal}) = \frac{Q_{Cu}}{M_{metal} \times 420\mu C \quad cm^{-2}}$$
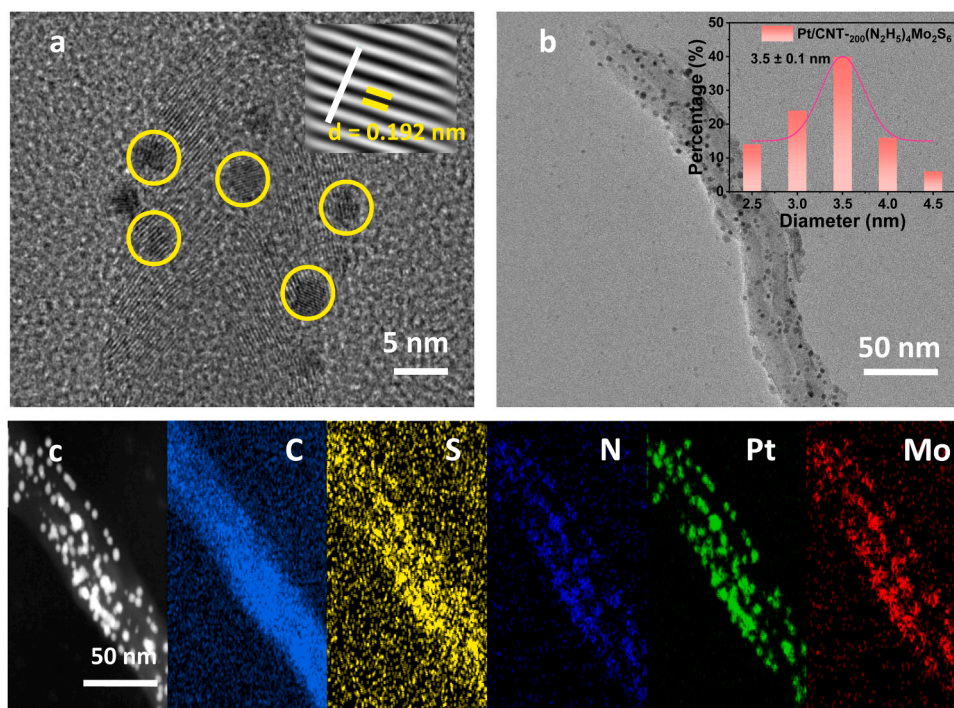
Fig. 1. (a) HR-TEM images of Pt/CNT-$_{200}$(N$_2$H$_5$)$_4$Mo$_2$S$_6$. (b) TEM image of Pt/CNT-$_{200}$(N$_2$H$_5$)$_4$Mo$_2$S$_6$. (c) HR-TEM image and corresponding elemental mappings of C, S, N, Pt, and Mo for Pt/CNT-$_{200}$(N$_2$H$_5$)$_4$Mo$_2$S$_6$.

2.5. Measurement of active sites (n)

The formula for calculating active sites (n) is as follows.

$$n = \frac{Q_{Cu}}{2 * F}$$

F is the Faraday constant (96485.3 C mol^{-1}).

2.6. Measurement of the turnover frequency (TOF)

The TOF (s^{-1}) value is calculated using the following formula.

$$TOF = \frac{I}{2 * n * F}$$

I (A) is the current of LSV. F is the Faraday constant (96485.3 C mol^{-1}). n is the number of active sites.

2.7. In situ Fourier transform infrared spectroscopy (FTIR) technique

Operation process of silicon plane gold plating film: preparation of gold plating solution. Solution A was prepared: 0.1222 g NaOH and 0.2286 g NaAuCl$_4$·2 H$_2$O were dissolved in 3 mL deionized water and dissolved by ultrasound for 1 h. Prepared B solution: 0.134 g NH$_4$Cl, 0.9468 g Na$_2$SO$_3$, 0.6202 g Na$_2$S$_2$O$_3$·5 H$_2$O dissolved in 50 mL deionized water, ultrasonic dispersion for 1 h. Solution A was mixed with solution B, and 50 mL of deionized water was added for full ultrasonic treatment for 2 h. Preparation for electroplating of silicon crystal: Soak the silicon crystal in Aqua regia (V(HCl): V(HNO$_3$) = 3:1) for 30 min, and then rinse with deionized water. Secondly, 50 µm Al$_2$O$_3$ powder was ground on the electrode cloth in the clockwise direction of silicon crystal electroplating for 10 min, and then cleaned with deionized water. Third, deionized water and acetone were alternately treated 5 times, respectively for 2 min, 1 min, 1 min, 1 min, 2 min. Fourth, take out the oxidizing solution (V(H$_2$SO$_4$): V(H$_2$O$_2$) = 3:1) and rinse with deionized water. Finally, the silicon coating was soaked in 40% NH$_4$F solution for 4–5 min and rinsed with deionized water. Gold film deposition: Put 15 mL gold plating solution into 25 mL beaker first, preheat it in

50–55 ℃ water bath for 2 min, then add 3.4 mL 2% HF. Secondly, the prepared silicon crystal is soaked in the above solution for 4–5 min, and finally washed with deionized water to obtain the gold plating layer.

2.8. In situ Raman technique

The *in situ* Raman spectrum was obtained by using a specially designed electrolytic cell consisting of the bottom working electrode, platinum wire as the opposite electrode and the reference electrode. A 60X objective confocal Raman microscope (inVia Qontor, Renishaw) was used. The laser wavelength used in all experiments was 532 nm.

2.9. AEM electrolysis

Disperse Pt/CNT-$_{200}$(N$_2$H$_5$)$_4$Mo$_2$S$_6$ powder in the mixture of absolute ethanol and nafion (1:0.05), and conduct ultrasonic treatment for 1 h to obtain a dispersion with a concentration of 1 mg/mL. Drop 100 µL onto the carbon paper (1 cm × 1 cm). Before use, degrease and pre treat in 0.1 M HCl solution to remove contaminants from the oxide layer on the instrument surface. Then, clip the anion exchange membrane (Sustainion X37–50) between the cathode and anode catalyst to build an electrolytic cell (Pt/CNT-$_{200}$(N$_2$H$_5$)$_4$Mo$_2$S$_6$||Pt/CNT-$_{200}$(N$_2$H$_5$)$_4$Mo$_2$S$_6$). At 60 ℃, 1 M KOH solution is continuously supplied to both sides of the electrolytic cell with a circulating pump at a flow rate of 1 s/mL.

2.10. Calculation Setup

We have employed the Vienna Ab Initio Package (VASP) to perform all the density functional theory (DFT) calculations within the generalized gradient approximation (GGA) using the PBE formulation. We have chosen the projected augmented wave (PAW) potentials to describe the ionic cores and take valence electrons into account using a plane wave basis set with a kinetic energy cutoff of 450 eV. Partial occupancies of the Kohn-Sham orbitals were allowed using the Gaussian smearing method and a width of 0.05 eV. The electronic energy was considered self-consistent when the energy change was smaller than 10^{-5} eV. A
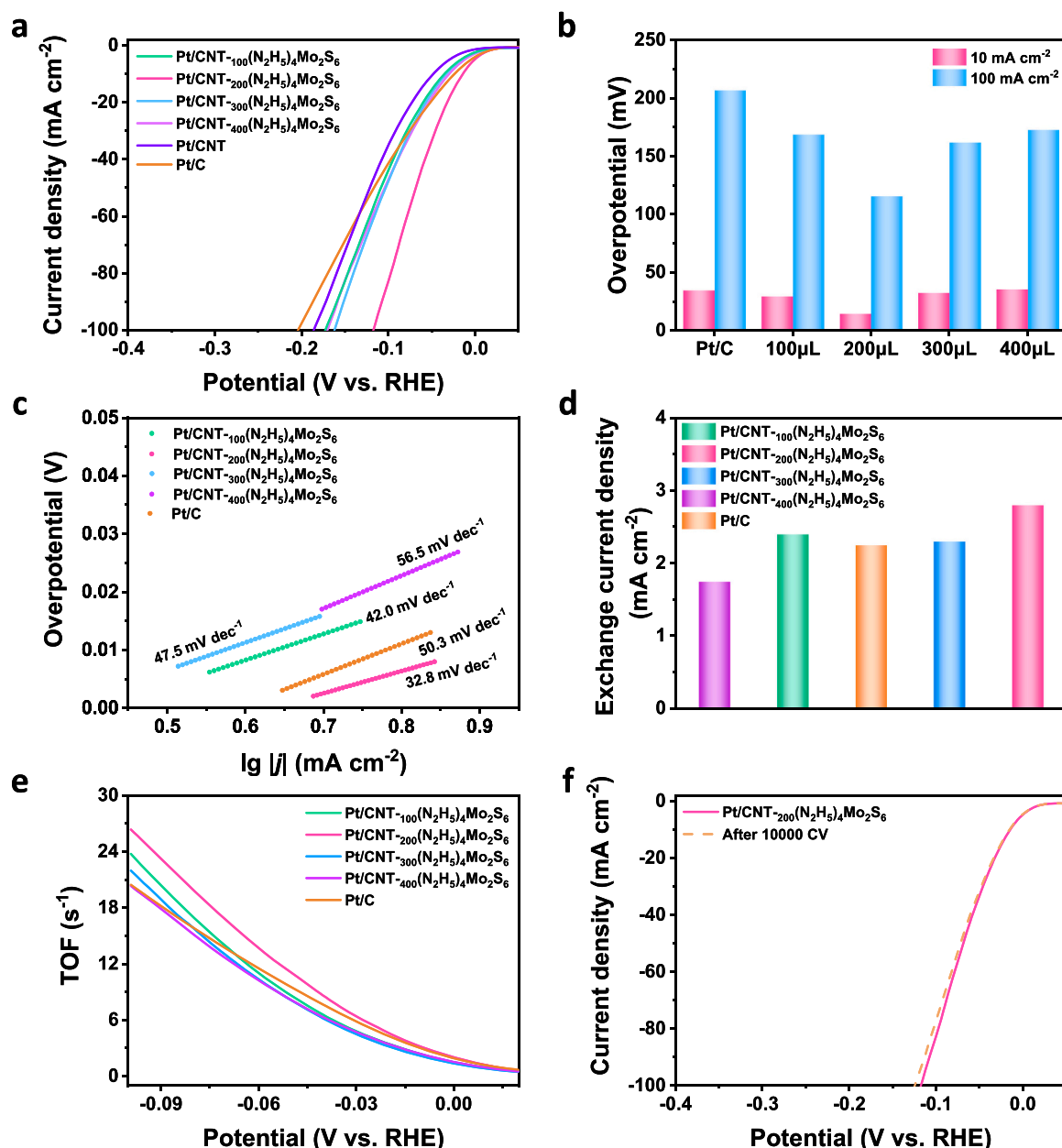
Fig. 2. (a) HER polarization curves of Pt/CNT-$_{100}$(N$_2$H$_5$)$_4$Mo$_2$S$_6$, Pt/CNT-$_{200}$(N$_2$H$_5$)$_4$Mo$_2$S$_6$, Pt/CNT-$_{300}$(N$_2$H$_5$)$_4$Mo$_2$S$_6$, Pt/CNT-$_{400}$(N$_2$H$_5$)$_4$Mo$_2$S$_6$, Pt/CNT and Pt/C in 1 M KOH + seawater. (b) Comparison of overpotential at 10 and 100 mA cm^{-2}. (c) Tafel plots derived from (a), (d) Comparison of exchange current density. (e) In 1 M KOH + seawater, Pt/CNT-$_{100}$(N$_2$H$_5$)$_4$Mo$_2$S$_6$, Pt/CNT-$_{200}$(N$_2$H$_5$)$_4$Mo$_2$S$_6$, Pt/CNT-$_{300}$(N$_2$H$_5$)$_4$Mo$_2$S$_6$, Pt/CNT-$_{400}$(N$_2$H$_5$)$_4$Mo$_2$S$_6$ and Pt/C TOF values. (f) Pt/CNT-$_{200}$(N$_2$H$_5$)$_4$Mo$_2$S$_6$ HER polarization curves before and after 10 k CV cycling in 1 M KOH + seawater.

geometry optimization was considered convergent when the force change was smaller than 0.03 eV/Å. Grimme's DFT-D3 methodology was used to describe the dispersion interactions. During structural optimizations, the $2 \times 2 \times 1$ Monkhorst-Pack k-point grid for Brillouin zone was used for k-point sampling for structures. The free energy (ΔG) for elemental reaction step were calculated as: $\Delta G = \Delta E + \Delta EZPE - T\Delta S$ where ΔE is the difference between the total energy, $\Delta EZPE$ and ΔS are the differences in the zero-point energy and the change of entropy, T is the temperature (T = 300 K in this work), respectively.

3. Results and discussion

3.1. Synthesis and structural characterizations

The Pt/CNT catalyst was synthesized by a simple solvent-free microwave reaction method (Fig. S1). As shown in Fig. S11, its morphology was studied by transmission electron microscopy (TEM). Pt nanoparticles were uniformly dispersed on the surface of CNT, where the average particle size of Pt nanoparticles was 3.5 ± 0.1 nm. Molecular metal chalcogenide complexes synthesized by a simple oil bath reaction. The color of the solution changes significantly when the reaction is kept at a constant temperature for 72 h at 130 °C. A clear solution is obtained after the reaction, with a small amount of black precipitate at the bottom. Fig. S2 shows the structure diagram of Mo$_2$S$_6^{4-}$ ion. The supernatant after the oil bath was added to the Pt/CNT electrocatalyst, stirred at 30 °C for 4 h, filtered and dried to obtain the Pt/CNT-(N$_2$H$_5$)$_4$Mo$_2$S$_6$ powder. The method can also be extended to the synthesis of a series of Pt/CNT-(N$_2$H$_5$)$_4$X$_2$Y$_6$ (X = Mo and Sn, Y = S, Se, and Te). The atomic ratios of Pt/CNT-$_{200}$(N$_2$H$_5$)$_4$Mo$_2$S$_6$ were detected by inductively coupled plasma atomic emission spectrometry (ICP-AES)

(Table S2). The morphology and structure of Pt/CNT-$_{200}$(N$_2$H$_5$)$_4$Mo$_2$S$_6$ were studied by transmission electron microscopy (TEM). As shown in Fig. 1b Pt nanoparticles are uniformly distributed on the surface of carbon nanotubes. High-resolution transmission electron microscopy (HR-TEM) shows that the lattice spacing of the nanoparticles is 0.192 nm (Fig. 1a), which is related to the (200) crystal plane of Pt. Furthermore, elemental mapping of Pt/CNT-$_{200}$(N$_2$H$_5$)$_4$Mo$_2$S$_6$ was also performed for energy dispersive X-ray spectroscopy (EDS) analysis, and as seen in Fig. 1c, C, S, N, Pt, and Mo are uniformly dispersed. As shown in Fig. S3a-c, X-ray powder diffraction (XRD) of Pt/CNT-$_{200}$(N$_2$H$_5$)$_4$Mo$_2$S$_6$ and Pt/CNT, it can be seen that the Pt/CNT modified by (N$_2$H$_5$)$_4$Mo$_2$S$_6$ has a distinct Mo peak. The chemical state and electronic structure of Pt/CNT-$_{200}$(N$_2$H$_5$)$_4$Mo$_2$S$_6$ were characterized by X-ray photoelectron spectroscopy (XPS). All XPS spectra were calibrated with C 1 s at 284.8 eV. Fig. S4 shows Pt 4 f, Mo 3d, C 1 s, N 1 s, O 1 s and S 2p peaks of Pt/CNT-$_{200}$(N$_2$H$_5$)$_4$Mo$_2$S$_6$. Fig. S5a shows the peak fitting of Pt 4 f. In Pt/CNT-$_{200}$(N$_2$H$_5$)$_4$Mo$_2$S$_6$, the dominant signals with the binding energy of 72.81 eV and 69.39 eV are assigned to Pt^0 4 f$_{5/2}$ and Pt^0 4 f$_{7/2}$, respectively. The binding energy of Pt/CNT-$_{200}$(N$_2$H$_5$)$_4$Mo$_2$S$_6$ and Pt/CNT were compared. In particular, the binding energy ratio of Pt^0 4 f to Pt/CNT has a positive shift of 0.4 eV, indicating that the Mo in (N$_2$H$_5$)$_4$Mo$_2$S$_6$ changes the electron cloud distribution of Pt, resulting in a shift of the Pt^0 4 f peak. The C 1 s spectrum of Pt/CNT-$_{200}$(N$_2$H$_5$)$_4$Mo$_2$S$_6$ showed different degrees of positive shift compared with Pt/CNT, indicating charge transfer between CNT and (N$_2$H$_5$)$_4$Mo$_2$S$_6$ (Fig. S5b). In addition, the synthetic Pt/CNT-$_{100}$(N$_2$H$_5$)$_4$Sn$_2$S$_6$ was also analyzed. It can be observed from Fig. S7b that Pt nanoparticles are uniformly distributed on the surface of carbon nanotubes with a lattice spacing of 0.194 nm (Fig. S7a) related to the (200) crystal plane of Pt. Compared with the XRD pattern of Pt/CNT-$_{100}$(N$_2$H$_5$)$_4$Sn$_2$S$_6$ and Pt/CNT (Fig. S3b), it can be seen that Pt/CNT modified by (N$_2$H$_5$)$_4$Sn$_2$S$_6$ has an obvious Sn peak. Fig. S8 shows Pt 4 f, Sn 3d, C 1 s, N 1 s, O 1 s, and S 2p peaks of Pt/CNT-$_{100}$(N$_2$H$_5$)$_4$Sn$_2$S$_6$. Fig. S9a shows the peak fitting of Pt 4 f. In Pt/CNT-$_{100}$(N$_2$H$_5$)$_4$Sn$_2$S$_6$, the dominant signals with binding energies of 72.34 eV and 68.95 eV are assigned to Pt^0 4 f$_{5/2}$ and Pt^0 4 f$_{7/2}$, respectively. The binding energy ratio of Pt^0 4 f to Pt/CNT has a positive shift of 0.2 eV, indicating that the modification of (N$_2$H$_5$)$_4$Sn$_2$S$_6$ leads to the charge transfer of Pt. The C 1 s spectrum of Pt/CNT-$_{100}$(N$_2$H$_5$)$_4$Sn$_2$S$_6$ showed different degrees of positive shift compared with Pt/CNT, indicating charge transfer between CNT and (N$_2$H$_5$)$_4$Sn$_2$S$_6$ (Fig. S9b). The morphology and structure of other Pt/CNT-(N$_2$H$_5$)$_4$X$_2$Y$_6$ (X = Mo and Sn, Y = S, Se, and Te) electrocatalysts were characterized by TEM and XRD. It was shown that a series of Pt/CNT-(N$_2$H$_5$)$_4$X$_2$Y$_6$ electrocatalysts were successfully synthesized (Fig. S12-15).

3.2. Electrochemical HER

We first evaluated the HER activity of the prepared electrocatalyst in 1 M KOH electrolyte in seawater at room temperature (25 °C). In this work, we demonstrate the direct electrolysis of alkaline and natural seawater, and filtering only to remove solids and microorganisms. Fig. 2a compares the polarization curves of the optimized Pt/CNT-$_X$(N$_2$H$_5$)$_4$Mo$_2$S$_6$, Pt/CNT and commercial Pt/CNT. Clearly, Pt/CNT-(N$_2$H$_5$)$_4$Mo$_2$S$_6$ showed the best HER activity, even superior to commercial Pt/C. The corresponding Tafel slopes and overpotentials (10 mA cm^{-2} and 100 mA cm^{-2}) were calculated and are shown in Fig. 2b-c. Pt/CNT-$_{200}$(N$_2$H$_5$)$_4$Mo$_2$S$_6$ has 20 mV overpotential at 10 mA cm^{-2}, which is better than Pt/CNT-$_{100}$(N$_2$H$_5$)$_4$Mo$_2$S$_6$ (28 mV), Pt/CNT-$_{300}$(N$_2$H$_5$)$_4$Mo$_2$S$_6$ (32 mV), Pt/CNT-$_{400}$(N$_2$H$_5$)$_4$Mo$_2$S$_6$ (36 mV) and commercial Pt/C (33 mV). Furthermore, it has 115 mV overpotential at 100 mA cm^{-2}, much lower than Pt/CNT-$_{100}$(N$_2$H$_5$)$_4$Mo$_2$S$_6$ (168 mV), Pt/CNT-$_{300}$(N$_2$H$_5$)$_4$Mo$_2$S$_6$ (161 mV), Pt/CNT-$_{400}$(N$_2$H$_5$)$_4$Mo$_2$S$_6$ (172 mV) and commercial Pt/C (206 mV) (Fig. 2b). The Tafel slope of Pt/CNT-$_{200}$(N$_2$H$_5$)$_4$Mo$_2$S$_6$ at 10 mA cm^{-2} is 32.8 mV dec^{-1}, which is lower than that of Pt/CNT-$_{100}$(N$_2$H$_5$)$_4$Mo$_2$S$_6$

(42.0 mV dec^{-1}), Pt/CNT-$_{300}$(N$_2$H$_5$)$_4$Mo$_2$S$_6$ (47.5 mV dec^{-1}), Pt/CNT-$_{400}$(N$_2$H$_5$)$_4$Mo$_2$S$_6$ (56.5 mV dec^{-1}) and commercial Pt/C (50.3 mV dec^{-1}) (Fig. 2c). The Tafel value is lower than 33 mV dec^{-1}, verifying that the H* adsorption/desorption is the rate-determining step of Pt/CNT-$_{200}$(N$_2$H$_5$)$_4$Mo$_2$S$_6$ during HER. In alkaline seawater HER, Pt/CNT-$_{200}$(N$_2$H$_5$)$_4$Mo$_2$S$_6$ electrocatalyst is competitive with electrocatalysts reported to date (Table S3). As shown in Fig. 2d, the exchange current density of Pt/CNT-$_{200}$(N$_2$H$_5$)$_4$Mo$_2$S$_6$ (2.8 mA cm^{-2}) was higher than that of Pt/CNT-$_{100}$(N$_2$H$_5$)$_4$Mo$_2$S$_6$ (2.5 mA cm^{-2}), Pt/CNT-$_{300}$(N$_2$H$_5$)$_4$Mo$_2$S$_6$ (2.3 mA cm^{-2}), Pt/CNT-$_{400}$(N$_2$H$_5$)$_4$Mo$_2$S$_6$ (1.9 mA cm^{-2}), and commercial Pt/C (2.5 mA cm^{-2}). The results show that Pt/CNT-$_{200}$(N$_2$H$_5$)$_4$Mo$_2$S$_6$ electrocatalyst has better hydrogen evolution performance. In addition, the electrochemically active surface area (ECSA) and the number of active sites (n) of Pt/CNT-(N$_2$H$_5$)$_4$Mo$_2$S$_6$ were calculated by Cu underpotential deposition (Cu-UPD) (Fig. S16-17). Compared to Pt/CNT-$_{100}$(N$_2$H$_5$)$_4$Mo$_2$S$_6$ (70.4 m^2/g), Pt/CNT-$_{300}$(N$_2$H$_5$)$_4$Mo$_2$S$_6$ (73.2 m^2/g), Pt/CNT-$_{400}$(N$_2$H$_5$)$_4$Mo$_2$S$_6$ (75.7 m^2/g) and commercial Pt/C (71.0 m^2/g), the Pt/CNT-$_{200}$(N$_2$H$_5$)$_4$Mo$_2$S$_6$ electrocatalyst had a lower ECSA (66.5 m^2/g) (Fig. S18a), while the Pt/CNT-$_{200}$(N$_2$H$_5$)$_4$Mo$_2$S$_6$ electrocatalyst also had a lower active site (Fig. S18b). The results indicate that modification of Pt/CNT with (N$_2$H$_5$)$_4$Mo$_2$S$_6$ covers a small number of active sites on the electrocatalyst surface. The electrochemical bilayer capacitance (C$_{dl}$) is linearly related to ECSA. We measured cyclic voltammetric curves (Fig. S19a-d) and calculated C$_{dl}$ (Fig. S20) in a specific voltage range (0.85–0.95 V *vs.* RHE) with different scan rates. The obtained results are in agreement with the Cu-UPD calculations. Fig. 2e shows that the turnover frequency (TOF) value of Pt/CNT-$_{200}$(N$_2$H$_5$)$_4$Mo$_2$S$_6$ is 20 s^{-1} at 100 mV, which is 2.6-fold that of commercial Pt/C (7.6 s^{-1}), 1.4-fold of Pt/CNT-$_{100}$(N$_2$H$_5$)$_4$Mo$_2$S$_6$ (14 s^{-1}), 1.7-fold of Pt/CNT-$_{300}$(N$_2$H$_5$)$_4$Mo$_2$S$_6$ (11.7 s^{-1}), and twice of Pt/CNT-$_{400}$(N$_2$H$_5$)$_4$Mo$_2$S$_6$ (9.8 s^{-1}). The Pt/CNT-$_{200}$(N$_2$H$_5$)$_4$Mo$_2$S$_6$ electrocatalyst was demonstrated to have the highest intrinsic catalytic activity. Moreover, the electrochemical impedance spectrum (EIS) was obtained under the action of equivalent circuit diagram (Fig. S31). Compared with other electrocatalysts, Pt/CNT-$_{200}$(N$_2$H$_5$)$_4$Mo$_2$S$_6$ has the highest charge transfer efficiency compared with other electrocatalysts (Fig. S21), verifying the excellent H* adsorption and desorption efficiency on Pt/CNT-$_{200}$(N$_2$H$_5$)$_4$Mo$_2$S$_6$ for better interface charge transfer. Stability is a very important factor for estimating the electrocatalysts′ cost in practical applications. During the 600 h stability test, the current density of Pt/CNT-$_{200}$(N$_2$H$_5$)$_4$Mo$_2$S$_6$ electrocatalyst did not fluctuate significantly (Fig. S22b), which proved that Pt/CNT-$_{200}$(N$_2$H$_5$)$_4$Mo$_2$S$_6$ maintained good stability in the harsh HER process. Fig. S42a TEM image shows that the morphology of Pt/CNT-$_{200}$(N$_2$H$_5$)$_4$Mo$_2$S$_6$ remains the same after the stability test. The XRD patterns of Pt/CNT-$_{200}$(N$_2$H$_5$)$_4$Mo$_2$S$_6$ before and after the stability test, as seen in Fig. S43a, did not change significantly. This demonstrates that Pt/CNT-$_{200}$(N$_2$H$_5$)$_4$Mo$_2$S$_6$ has excellent structural stability. Furthermore, Pt/CNT-$_{200}$(N$_2$H$_5$)$_4$Mo$_2$S$_6$ showed the highest current density compared to other electrocatalysts (Fig. S22). Cyclic voltammetry was also used for catalytic stability testing (Fig. 2f), where the Pt/CNT-$_{200}$(N$_2$H$_5$)$_4$Mo$_2$S$_6$ possess an overpotential decay of 2 mV (10 mA cm^{-2}) after 10 k cycles. The Pt/CNT-$_{200}$(N$_2$H$_5$)$_4$Mo$_2$S$_6$ electrocatalyst was demonstrated to have high electrocatalytic stability. The electrochemical performance of Pt/CNT-$_{100}$(N$_2$H$_5$)$_4$Sn$_2$S$_6$ was tested for comparison with commercial Pt/C. Fig. S23a compares the polarization curves of Pt/CNT-$_{100}$(N$_2$H$_5$)$_4$Sn$_2$S$_6$, Pt/CNT and commercial Pt/C. The HER activity of Pt/CNT-$_{100}$(N$_2$H$_5$)$_4$Sn$_2$S$_6$ electrocatalyst was superior to that of commercial Pt/C. The Pt/CNT-$_{100}$(N$_2$H$_5$)$_4$Sn$_2$S$_6$ electrocatalyst has an overpotential of 26 mV at 10 mA cm^{-2} and 182 mV at 100 mA cm^{-2} (Fig. S23b). The Tafel slope of the Pt/CNT-$_{100}$(N$_2$H$_5$)$_4$Sn$_2$S$_6$ electrocatalyst at 10 mA cm^{-2} was 41.4 mV dec^{-1} (Fig. S23c); the exchange current density was 2.6 mA cm^{-2} (Fig. S23d). Calculate the electrochemical active surface area (69.5 m^2/g) of Pt/CNT-$_{100}$(N$_2$H$_5$)$_4$Sn$_2$S$_6$ (Fig. S26a), and the number of active sites decreases (Fig. S26b). From the cyclic voltammetry curves measured at

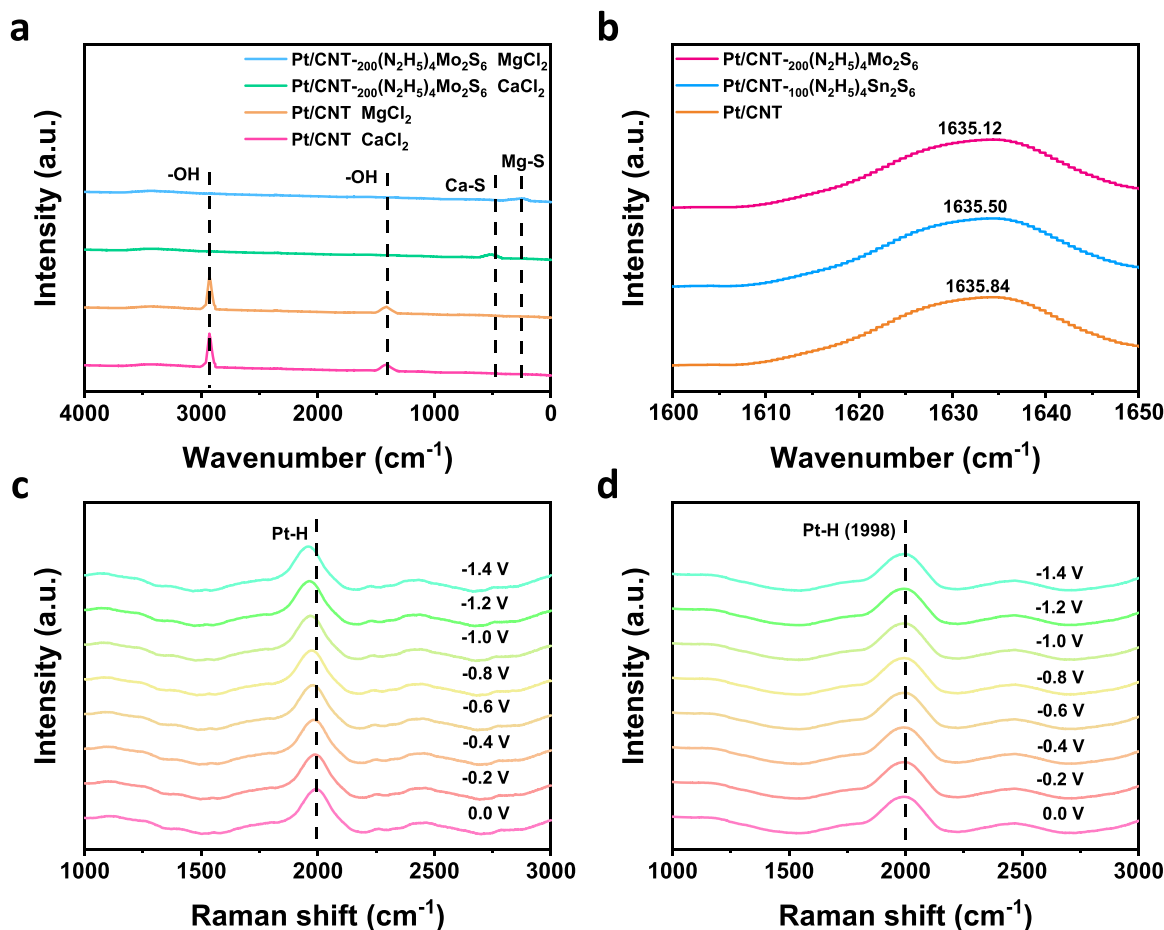**Fig. 3.** *In situ* FTIR spectra (a) Pt/CNT-$_{200}$(N$_2$H$_5$)$_4$Mo$_2$S$_6$ was compared with Pt/CNT in different solutions. (b) At the same voltage, different materials are compared. *In situ* Raman spectra of (c, d) Pt/CNT-$_{200}$(N$_2$H$_5$)$_4$Mo$_2$S$_6$ and Pt/CNT at different potentials. The Raman signal on the catalyst surface is Pt-H: ~1998 cm^{-1}.

different scan rates (Fig. S27), the C$_{dl}$ was calculated (Fig. S28). As shown in Fig. S23e, the Pt/CNT-$_{100}$(N$_2$H$_5$)$_4$Sn$_2$S$_6$ electrocatalyst has a TOF of 17 s^{-1} at 10 mV overpotential, which is 2.2-fold higher than that of commercial Pt/C. The electrochemical impedance spectroscopy (Fig. S29) shows that the charge transfer rate of Pt/CNT-$_{100}$(N$_2$H$_5$)$_4$Sn$_2$S$_6$ is faster than that of Pt/C. During the 600 h stability test, the current density of Pt/CNT-$_{100}$(N$_2$H$_5$)$_4$Sn$_2$S$_6$ did not fluctuate significantly, which proves that the electrocatalyst has good stability (Fig. S30). Fig. S42b TEM image shows that the morphology of Pt/CNT-$_{100}$(N$_2$H$_5$)$_4$Sn$_2$S$_6$ did not change significantly after the stability test. The XRD patterns of Pt/CNT-$_{100}$(N$_2$H$_5$)$_4$Sn$_2$S$_6$ before and after the stability test, as seen in Fig. S43b, did not change significantly. This demonstrates that Pt/CNT-$_{100}$(N$_2$H$_5$)$_4$Sn$_2$S$_6$ has excellent structural stability.

The Pt/CNT-$_{100}$(N$_2$H$_5$)$_4$Sn$_2$S$_6$ electrocatalyst showed an overpotential decay of 3 mV (10 mA cm^{-2}) after 10 k cycles (Fig. S23f), again demonstrating the good stability of the electrocatalyst. Furthermore, the electrochemical performance of a series of Pt/CNT-(N$_2$H$_5$)$_4$X$_2$Y$_6$ (X = Mo and Sn, Y═S, Se and Te) electrocatalysts was tested (Fig. S34-37). As shown in Fig. S35 and Fig. S37, the overpotentials corresponding to each catalyst at 10 mA cm^{-2} and 100 mA cm^{-2}, respectively, are compared. It can be seen that Pt/CNT-$_{200}$(N$_2$H$_5$)$_4$Mo$_2$S$_6$ and Pt/CNT-$_{100}$(N$_2$H$_5$)$_4$Sn$_2$S$_6$ exhibit superior performance.

Above, the HER activity of each electrocatalyst was compared in 1 M KOH seawater electrolyte. Moreover, we tested the HER performance of Pt/CNT-$_{200}$(N$_2$H$_5$)$_4$Mo$_2$S$_6$ and Pt/CNT-$_{100}$(N$_2$H$_5$)$_4$Sn$_2$S$_6$ in natural seawater. The polarization curves of the electrocatalysts under different electrolyte solutions are shown in Fig. S32a and Fig. S33a. Pt/

CNT-$_{200}$(N$_2$H$_5$)$_4$Mo$_2$S$_6$ and Pt/CNT-$_{100}$(N$_2$H$_5$)$_4$Sn$_2$S$_6$ have better HER activity in 1 M KOH seawater electrolyte. Under natural seawater, the overpotential of Pt/CNT-$_{200}$(N$_2$H$_5$)$_4$Mo$_2$S$_6$ was 22 mV and 119 mV at 10 mA cm^{-2} and 100 mA cm^{-2}, respectively (Fig. S32b); the overpotential of Pt/CNT-$_{100}$(N$_2$H$_5$)$_4$Sn$_2$S$_6$ was 30 mV and 188 mV at 10 mA cm^{-2} and 100 mA cm^{-2}, respectively (Fig. S33b).

3.3. Insights into the underlying HER mechanism

In situ Fourier transform infrared spectroscopy (FTIR) was used to study the role of Pt/CNT-$_{200}$(N$_2$H$_5$)$_4$Mo$_2$S$_6$ electrocatalyst in the electrolysis process of alkaline seawater. The test was performed in a mixed electrolyte solution of 1 M KOH + seawater + 0.1 M MgCl$_2$ (or 0.1 M CaCl$_2$) (supernatant). As shown in Fig. 3a, when Pt/CNT-$_{200}$(N$_2$H$_5$)$_4$Mo$_2$S$_6$ is used as an electrocatalyst, obvious vibration peaks of the Mg-S bond (~300 nm^{-1}) or Ca-S bond (~500 nm^{-1}) will appear during the reaction (Fig. S39a-b). Similarly, similar phenomena occur with Pt/CNT-$_{100}$(N$_2$H$_5$)$_4$Sn$_2$S$_6$ (Fig. S38). However, the unmodified Pt/CNT showed obvious Mg-OH or Ca-OH characteristic peaks during the reaction. Comparing the electrocatalysts before and after the reaction, no white precipitate appeared on the surface of the modified Pt/CNT, while a white precipitate appeared on the surface of the Pt/CNT. The results show that the bonding ability of metal cations (Mg^{2+}, Ca^{2+}) to OH$^-$ is weakened under the influence of coordination, and S in (N$_2$H$_5$)$_4$Mo$_2$S$_6$ combines with Mg^{2+} and Ca^{2+} to form ligand compounds. In addition, ion product (Q) is less than the precipitation equilibrium constant (K$_{sp, Mg(OH)2}$, K$_{sp, Ca(OH)2}$), which proves that the formation of coordination compounds under the influence of coordination effectively prevents the formation of insoluble precipitation. The
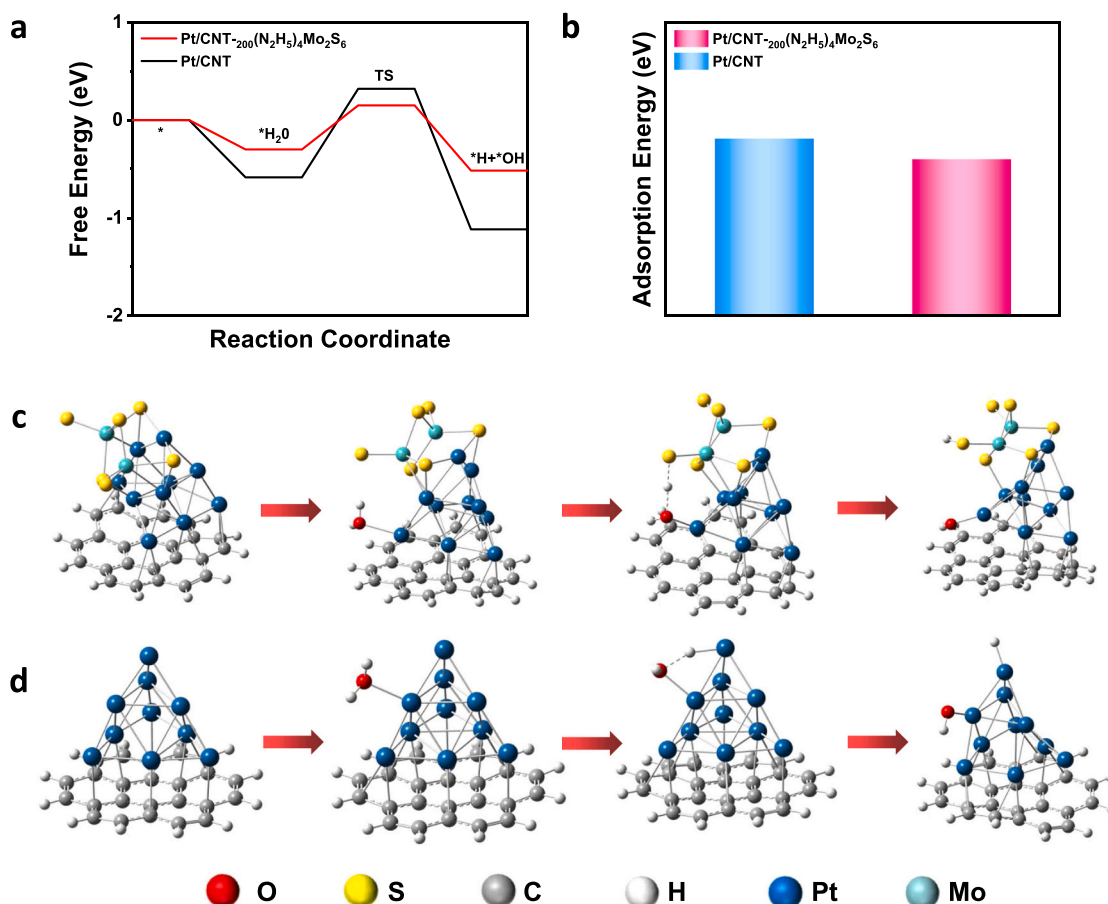
Fig. 4. (a) Hydrogen adsorption free energy of Pt/CNT-$_{200}$(N$_2$H$_5$)$_4$Mo$_2$S$_6$ and Pt/CNT. (b) The H$_2$O adsorption free energy of Pt/CNT-$_{200}$(N$_2$H$_5$)$_4$Mo$_2$S$_6$ and Pt/CNT. (c) Schematic diagram of reaction mechanism proposed on Pt/CNT-$_{200}$(N$_2$H$_5$)$_4$Mo$_2$S$_6$. (d) Schematic diagram of reaction mechanism proposed on Pt/CNT.

accelerated water evolution mechanism on Pt/CNT-$_{200}$(N$_2$H$_5$)$_4$Mo$_2$S$_6$ is discovered by *in situ* FTIR. From Fig. 3b, the H-O-H bending vibration peak on Pt/CNT-$_{200}$(N$_2$H$_5$)$_4$Mo$_2$S$_6$ (1635.1 cm^{-1}) is lower than the wave number of Pt/CNT-$_{100}$(N$_2$H$_5$)$_4$Sn$_2$S$_6$ (1635.5 cm^{-1}) and Pt/CNT (1635.8 cm^{-1}), indicating that the modified Pt/CNT electrocatalyst promotes the occurrence of water decomposition. As the applied voltage becomes more negative, the number of H-O-H bending vibration peak waves of Pt/CNT-$_{200}$(N$_2$H$_5$)$_4$Mo$_2$S$_6$ becomes lower and lower (Fig. S40a). It shows that the O-H bond in the electrolyte becomes weaker and more easily broken. This phenomenon provides sufficient H* for the Heyrovsky step, increasing the rate of the HER and ensuring the excellent performance of the Pt/CNT-$_{200}$(N$_2$H$_5$)$_4$Mo$_2$S$_6$. The active sites of hydrogen overflow in alkaline seawater were studied by *in situ* Raman spectroscopy. As shown in Fig. 3c, the Pt-H peak appears at 1998 cm^{-1}, indicating that the H* produced during the Volmer step was adsorbed on the Pt site. During the reaction, as the applied voltage becomes more negative, the wave number of the Pt-H signal peak decreases and is red-shifted. Furthermore, the peak area of the Pt-H signal increases, and more H* is enriched on the surface of the Pt. Reaction mechanism of the electrocatalyst in alkaline electrolyte: Pt promotes the hydrogen bond breakage during hydrolysis (H$_2$O + e$^-$ → H* + OH$^-$), while the H$_2$ desorption step (H* + H$_2$O + e$^-$ → OH$^-$ + H$_2$) can be performed quickly at the Pt site.

To further analyze the excellent catalytic activity of Pt/CNT-$_{200}$(N$_2$H$_5$)$_4$Mo$_2$S$_6$ electrocatalyst, we compared the catalytic activity of two nano-electrocatalysts in HER reaction by DFT study. The optimized structural models of Pt/CNT-$_{200}$(N$_2$H$_5$)$_4$Mo$_2$S$_6$ and Pt/CNT were determined (Fig. S44a-b). According to the electrocatalytic performance, we derived that this electrocatalyst in an alkaline solution follows a Volmer-Heyrovsky mechanism: the Volmer step (water dissociation) and the Heyrovsky step (hydrogen desorption). Firstly, the adsorption and dissociation-free energies of water molecules on the two electrocatalysts were compared. As can be seen from the calculation results in Fig. 4a, the Gibbs free energy of adsorption (ΔG_{H2O}) for the water of Pt/CNT-$_{200}$(N$_2$H$_5$)$_4$Mo$_2$S$_6$ electrocatalyst is lower than that of Pt/CNT, which is more conducive to the adsorption of H* . In addition, in the Volmer step, Pt is used as the adsorption site of OH* , and the adsorption free energy of Pt/CNT-$_{200}$(N$_2$H$_5$)$_4$Mo$_2$S$_6$ and Pt/CNT electrocatalysts (ΔG_{H*}), DFT calculation shows that Pt/CNT ΔG_{H*} is closer to the thermo-neutral state in comparison, while Pt/CNT-$_{200}$(N$_2$H$_5$)$_4$Mo$_2$S$_6$ has a large Gibbs adsorption free energy, which reveals that it is not conducive to the adsorption of H* . Combined with the experimental results and DFT analysis, it can be concluded that the modified Pt/CNT promotes the decomposition of water, and makes the adsorption and desorption effect of H* better. Based on the results of DFT and *in situ* experiments above, we proposed the catalytic mechanism of the electrocatalyst's participation in HER reaction in alkaline seawater, as shown in Fig. 4c-d: the Pt atom acts as a site for water adsorption and dissociation, H* is strongly adsorbed by Pt, then H* intermediate is transferred to Pt and finally, the desorption of H$_2$ occurs at the Pt site.

3.4. Performance in alkaline seawater electrolyzers device

Finally, inspired by the remarkable HER activity and stability of Pt/CNT-$_{200}$(N$_2$H$_5$)$_4$Mo$_2$S$_6$ electrocatalyst in a three-electrode system, we further evaluated the performance of Pt/CNT-$_{200}$(N$_2$H$_5$)$_4$Mo$_2$S$_6$ electrocatalyst with a loading capacity of 0.1 mg cm^{-2}. Work in actual AEM electrolytic cell at 60 °C. The hydrogen evolution reaction (HER)
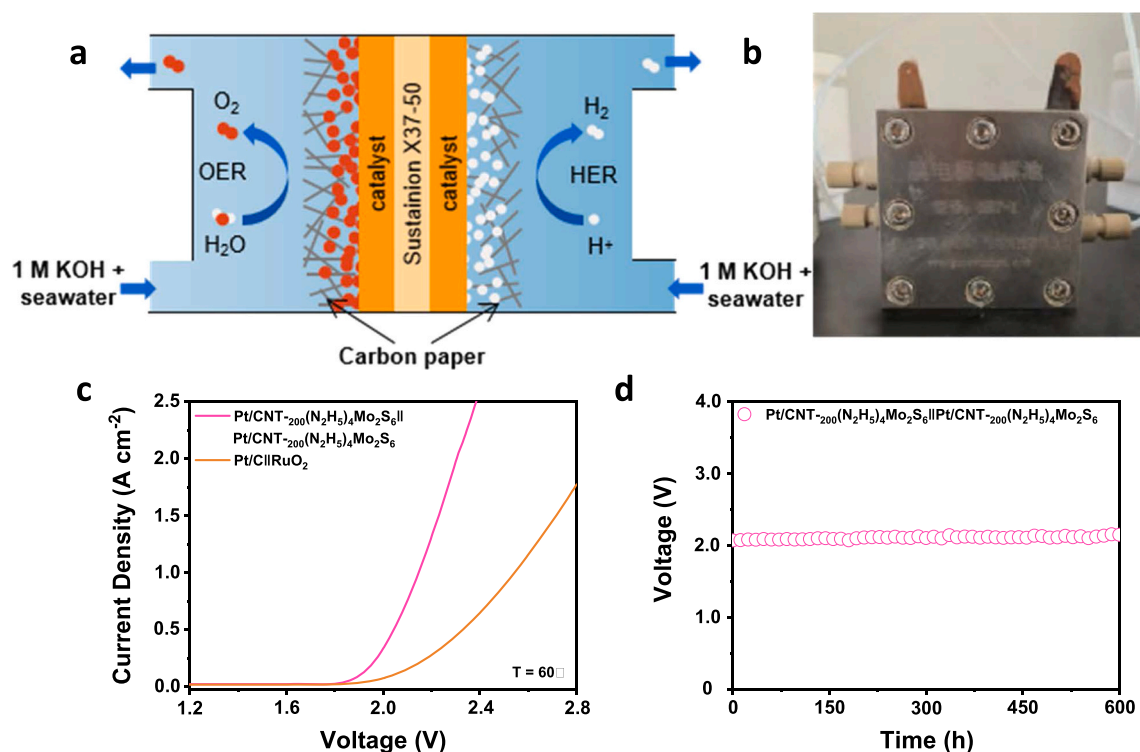
Fig. 5. Performance of Pt/CNT-$_{200}$(N$_2$H$_5$)$_4$Mo$_2$S$_6$ electrocatalyst on AEM electrolyzer at 60 °C. a,b, Schematic (a) and photograph (b) of the AEM device. (c) Polarization curves of Pt/CNT-$_{200}$(N$_2$H$_5$)$_4$Mo$_2$S$_6$||Pt/CNT-$_{200}$(N$_2$H$_5$)$_4$Mo$_2$S$_6$ and Pt/C||RuO$_2$ the in AEM electrolyser. (d) Chronopotentiometry testing of Pt/CNT-$_{200}$(N$_2$H$_5$)$_4$Mo$_2$S$_6$||Pt/CNT-$_{200}$(N$_2$H$_5$)$_4$Mo$_2$S$_6$ at 1 A cm^{-2}.

activity of Pt/CNT-$_{200}$(N$_2$H$_5$)$_4$Mo$_2$S$_6$ is higher than that of commercial Pt/C electrocatalysts. We built an AEM electrolyzer supported by Pt/CNT-$_{200}$(N$_2$H$_5$)$_4$Mo$_2$S$_6$ electrocatalyst on carbon paper (Fig. 5a-b). The voltage and current characteristics of Fig. 5c curve clearly show that Pt/CNT-$_{200}$(N$_2$H$_5$)$_4$Mo$_2$S$_6$||Pt/CNT-$_{200}$(N$_2$H$_5$)$_4$Mo$_2$S$_6$ electrolytic cell has better water electrolysis activity than Pt/C||RuO$_2$ electrolytic cell. Specifically, Pt/CNT-$_{200}$(N$_2$H$_5$)$_4$Mo$_2$S$_6$||Pt/CNT-$_{200}$(N$_2$H$_5$)$_4$Mo$_2$S$_6$ electrolytic cell (at room temperature) is only about 2.0 V, which can reach 1 A cm^{-2} (Fig. 5c). In practical applications, the stability of the electrocatalyst may play a more important role than its activity. Therefore, we evaluated the Pt/CNT-$_{200}$(N$_2$H$_5$)$_4$Mo$_2$S$_6$||Pt/CNT-$_{200}$(N$_2$H$_5$)$_4$Mo$_2$S$_6$ stability of electrolyzer. During the 600 h electrochemical test, the battery voltage only fluctuated slightly, indicating that the electrocatalyst also had excellent stability in the AEM electrolyzer (Fig. 5d).

4. Conclusion

In summary, we demonstrated that the formation of insoluble precipitates can be effectively prevented during the direct electrolysis of alkaline seawater, thus significantly improving the stability of hydrogen evolution at the cathode. This phenomenon is due to the coordination effect of Pt/CNT-$_{200}$(N$_2$H$_5$)$_4$Mo$_2$S$_6$ electrocatalyst on the contact with cations in solution. The formation of coordination compounds reduces the formation of insoluble precipitates. The Pt/CNT-$_{200}$(N$_2$H$_5$)$_4$Mo$_2$S$_6$ electrocatalyst was used as the cathode to operate stably in seawater. The alkaline AEM electrolyzer with modified Pt/CNT electrocatalyst has good stability at 1.0 A cm^{-2} for 600 h and exhibits an industrially required current density of 1.0 A cm^{-2} at 2.0 V and 60 °C. This study unveils molecular metal chalcogenide complexes to modify electrocatalysts as an effective strategy to prevent the formation of insoluble precipitates on the catalyst surface for hydrogen production and other reduction reaction applications at the large current density in direct alkaline seawater.

CRediT authorship contribution statement

Liang Zhao: Investigation, Conceptualization, Data curation, Formal analysis, Writing – original draft. **Shuanglong Zhou:** Conceptualization, Data curation, Writing – review & editing. **Zheng Lv:** Formal analysis, Data curation, Writing – original draft, Funding acquisition. **Wenxia Xu:** Investigation, Conceptualization, Data curation. **Jiaxin Liu:** Data curation, Formal analysis. **Ziyi Liu:** Formal analysis, Writing – review & editing. **Qi Zhang:** Writing – review & editing, Supervision. **Jianping Lai**: Investigation, Conceptualization, Validation, Writing – review & editing, Supervision. **Lei Wang:** Resources, Funding acquisition, Validation, Supervision.

Declaration of Competing Interest

The authors declare that they have no known competing financial interests or personal relationships that could have appeared to influence the work reported in this paper.

Data Availability

No data was used for the research described in the article.

(ZR2020ZD09).

Appendix A. Supporting information

Supplementary data associated with this article can be found in the online version at doi:10.1016/j.apcatb.2023.122996.

References

[1] W. Tong, M. Forster, F. Dionigi, S. Dresp, R. Sadeghi Erami, P. Strasser, A.J. Cowan, P. Farràs, Electrolysis of low-grade and saline surface water, Nat. Energy 5 (2020) 367–377, https://doi.org/10.1038/s41560-020-0550-8.

[2] K. Zuo, X. Zhang, X. Huang, E.F. Oliveira, H. Guo, T. Zhai, W. Wang, P.J.J. Alvarez, M. Elimelech, P.M. Ajayan, J. Lou, Q. Li, Ultrahigh resistance of hexagonal boron nitride to mineral scale formation, Nat. Commun. 13 (2022) 4523, https://doi.org/10.1038/s41467-022-32193-4.

[3] L. Yu, Q. Zhu, S. Song, B. McElhenny, D. Wang, C. Wu, Z. Qin, J. Bao, Y. Yu, S. Chen, Z. Ren, Non-noble metal-nitride based electrocatalysts for high-performance alkaline seawater electrolysis, Nat. Commun. 10 (2019) 5106, https://doi.org/10.1038/s41467-019-13092-7.

[4] F. Zhang, L. Yu, L. Wu, D. Luo, Z. Ren, Rational design of oxygen evolution reaction catalysts for seawater electrolysis, Trends Chem. 3 (2021) 485–498, https://doi.org/10.1016/j.trechm.2021.03.003.

[5] F. Sun, J. Qin, Z. Wang, M. Yu, X. Wu, X. Sun, J. Qiu, Energy-saving hydrogen production by chlorine-free hybrid seawater splitting coupling hydrazine degradation, Nat. Commun. 12 (2021) 4182, https://doi.org/10.1038/s41467-021-24529-3.

[6] Y. Gao, Y. Xue, L. Qi, C. Xing, X. Zheng, F. He, Y. Li, Rhodium nanocrystals on porous graphdiyne for electrocatalytic hydrogen evolution from saline water, Nat. Commun. 13 (2022) 5227, https://doi.org/10.1038/s41467-022-32937-2.

[7] I.A. Digdaya, I. Sullivan, M. Lin, L. Han, W.H. Cheng, H.A. Atwater, C. Xiang, A direct coupled electrochemical system for capture and conversion of CO₂ from oceanwater, Nat. Commun. 11 (2020) 4412, https://doi.org/10.1038/s41467-020-18232-y.

[8] H. You, D. Wu, D. Si, M. Cao, F. Sun, H. Zhang, H. Wang, T.F. Liu, R. Cao, Monolayer niIr-layered double hydroxide as a long-lived efficient oxygen evolution catalyst for seawater splitting, J. Am. Chem. Soc. 21 (2022) 9254–9263, https://doi.org/10.1021/jacs.2c00242.

[9] Y.Y. Ma, C.X. Wu, X.J. Feng, H.Q. Tan, L.K. Yan, High efficient hydrogen evolution from seawater by a low-cost and stable CoMoP@C electrocatalyst superior to Pt/C, Energy Environ. Sci. 10 (2017) 788–798, https://doi.org/10.1039/C6EE03768B.

[10] X. Lu, J. Pan, E.C. Lovell, T.H. Tan, Y.H. Ng, R. Amal, A sea-change: manganese doped nickel/nickel oxide electrocatalysts for hydrogen generation from seawater, Energy Environ. Sci. 11 (2018) 1898–1910, https://doi.org/10.1039/C8EE00976G.

[11] M.A. Khan, T. Al-Attas, S. Roy, M.M. Rahman, N. Ghaffour, V. Thangadurai, S. Larter, J. Hu, P.M. Ajayan, M.G. Kibria, Seawater electrolysis for hydrogen production: A solution looking for a problem, Energy Environ. Sci. 14 (2021) 4831–4839, https://doi.org/10.1039/D1EE00870F.

[12] S. Dresp, T. Ngo Thanh, M. Klingenhof, S. Brueckner, P. Hauke, P. Strasser, Efficient direct seawater electrolysers using selective alkaline NiFe-LDH as OER catalyst in asymmetric electrolyte feeds, Energy Environ. Sci. 13 (2020) 1725–1729, https://doi.org/10.1039/D0EE01125H.

[13] W. Yu, Z. Chen, Y. Fu, W. Xiao, T. Ma, B. Dong, Y. Chai, Z. Wu, L. Wang, Co-Mo microcolumns decorated with trace Pt for large current density hydrogen generation in alkaline seawater, Appl. Catal. B Environ. 317 (2022), 121762, https://doi.org/10.1016/j.apcatb.2022.121762.

[14] T. Ma, W. Xu, B. Li, X. Chen, J. Zhao, S. Wan, K. Jiang, S. Zhang, Z. Wang, Z. Tian, Z. Lu, L. Chen, The critical role of additive sulfate for stable alkaline seawater oxidation on Ni-based electrode, Angew. Chem. Int. Ed. 60 (2021) 22740–22744, https://doi.org/10.1002/anie.202110355.

[15] W. Zang, T. Sun, T. Yang, S. Xi, M. Waqar, Z. Kou, Z. Lyu, Y.P. Feng, J. Wang, S. J. Pennycook, Efficient hydrogen evolution of oxidized Ni-N₃ defective sites for alkaline freshwater and seawater electrolysis, Adv. Mater. 33 (2020) 2003846, https://doi.org/10.1002/adma.202003846.

[16] L. Wu, F. Zhang, S. Song, M. Ning, Q. Zhu, J. Zhou, G. Gao, Z. Chen, Q. Zhou, X. Xing, T. Tong, Y. Yao, J. Bao, L. Yu, S. Chen, Z. Ren, Efficient alkaline water/seawater hydrogen evolution by a nanorod-nanoparticle-structured Ni-MoN catalyst with fast water-dissociation kinetics, Adv. Mater. 34 (2022) 2201774, https://doi.org/10.1002/adma.202201774.

[17] H. Jin, X. Wang, C. Tang, A. Vasileff, L. Li, A. Slattery, S.Z. Qiao, Stable and highly efficient hydrogen evolution from seawater enabled by an unsaturated nickel surface nitride, Adv. Mater. 33 (2021) 2007508, https://doi.org/10.1002/adma.202007508.

[18] J. Chang, G. Wang, Z. Yang, B. Li, Q. Wang, R. Kuliiev, N. Orlovskaya, M. Gu, Y. Du, G. Wang, Y. Yang, Dual-doping and synergism toward high-performance seawater electrolysis, Adv. Mater. 13 (2021) 2101425, https://doi.org/10.1002/adma.202101425.

[19] Y. Zhao, B. Jin, Y. Zheng, H. Jin, Y. Jiao, S.Z. Qiao, Charge state manipulation of cobalt selenide catalyst for overall seawater electrolysis, Adv. Energy Mater. 15 (2018) 1801926, https://doi.org/10.1002/aenm.201801926.

[20] S. Dresp, F. Dionigi, S. Loos, J. Ferreira de Araujo, C. Spöri, M. Gliech, H. Dau, P. Strasser, Direct electrolytic splitting of seawater: activity, selectivity, degradation, and recovery studied from the molecular catalyst structure to the electrolyzer cell level, Adv. Energy Mater. 8 (2018) 1800338, https://doi.org/10.1002/aenm.201800338.

[21] L. Yu, L. Wu, S. Song, B. McElhenny, F. Zhang, S. Chen, Z. Ren, Hydrogen generation from seawater electrolysis over a sandwich-like NiCoN|NixP|NiCoN microsheet arrays catalyst, ACS Energy Lett. 5 (8) (2020) 2681–2689, https://doi.org/10.1002/acsenergylett.0c01244.

[22] S. Dresp, F. Dionigi, M. Klingenhof, P. Strasser, Direct electrolytic splitting of seawater: opportunities and challenges, ACS Energy Lett. 4 (2019) 933–942, https://doi.org/10.1021/acsenergylett.9b00220.

[23] J. Zhu, Y. Tu, L. Cai, H. Ma, Y. Chai, L. Zhang, W. Zhang, Defect-assisted anchoring of Pt single atoms on MoS₂ nanosheets produces high-performance catalyst for industrial hydrogen evolution reaction, Small 18 (2022), e2104824, https://doi.org/10.1002/smll.202104824.

[24] K.L. Zhou, Z. Wang, C.B. Han, X. Ke, C. Wang, Y. Jin, Q. Zhang, J. Liu, H. Wang, H. Yan, Platinum single-atom catalyst coupled with transition metal/metal oxide heterostructure for accelerating alkaline hydrogen evolution reaction, Nat. Commun. 12 (2021) 3783, https://doi.org/10.1038/s41467-021-24079-8.

[25] Y. Sun, Y. Zang, W. Tian, X. Yu, J. Qi, L. Chen, X. Liu, H. Qiu, Plasma-induced large-area N,Pt-doping and phase engineering of MoS₂ nanosheets for alkaline hydrogen evolution, Energy Environ. Sci. 15 (2022) 1201–1210, https://doi.org/10.1039/d1ee03825g.

[26] A. Nairan, C. Liang, S.-W. Chiang, Y. Wu, P. Zou, U. Khan, W. Liu, F. Kang, S. Guo, J. Wu, C. Yang, Proton selective adsorption on Pt–Ni nano-thorn array electrodes for superior hydrogen evolution activity, Energy Environ. Sci. 14 (2021) 1594–1601, https://doi.org/10.1039/d1ee00106j.

[27] Z. Wang, B. Xiao, Z. Lin, Y. Xu, Y. Lin, F. Meng, Q. Zhang, L. Gu, B. Fang, S. Guo, W. Zhong, PtSe₂/Pt heterointerface with reduced coordination for boosted hydrogen evolution reaction, Angew. Chem. Int. Ed. 60 (2021) 23388–23393, https://doi.org/10.1002/anie.202110335.

[28] S.Y. Pang, W.F. Io, J. Hao, Facile atomic-level tuning of reactive metal–support interactions in the Pt QDs@ HF-Free MXene heterostructure for accelerating pH-Universal hydrogen evolution reaction, Adv. Sci. 8 (2021) 2102207, https://doi.org/10.1002/advs.202102207.

[29] C. Zhang, Y. Cui, Y. Wang, L. Lu, S. Yu, Z. Meng, Y. Wu, Y. Li, Y. Wang, H. Tian, W. Zheng, Highly conductive amorphous pentlandite anchored with ultrafine platinum nanoparticles for efficient pH-Universal hydrogen evolution reaction, Adv. Funct. Mater. 31 (2021) 2105372, https://doi.org/10.1002/adfm.202105372.

[30] H. Xie, Z. Zhao, T. Liu, Y. Wu, C. Lan, W. Jiang, L. Zhu, Y. Wang, D. Yang, Z. Shao, A membrane-based seawater electrolyser for hydrogen generation, Nature 612 (2022) 673–678, https://doi.org/10.1038/s41586-022-05379-5.

[31] J. Guo, Y. Zheng, Z. Hu, C. Zheng, J. Mao, K. Du, M. Jaroniec, S. Qiao, T. Ling, Direct seawater electrolysis by adjusting the local reaction environment of a catalyst, Nat. Energy 8 (2023) 264–272, https://doi.org/10.1038/s41560-023-01195-x.

[32] Z. Jia, K. Nomoto, Q. Wang, C. Kong, L. Sun, L.C. Zhang, S.X. Liang, J. Lu, J. J. Kruzic, A self-supported high-entropy metallic glass with a nanosponge architecture for efficient hydrogen evolution under alkaline and acidic conditions, Adv. Funct. Mater. 31 (2021) 2101586, https://doi.org/10.1002/adfm.202101586.

[33] W. Zhang, B. Huang, K. Wang, W. Yang, F. Lv, N. Li, Y. Chao, P. Zhou, Y. Yang, Y. Li, J. Zhou, W. Zhang, Y. Du, D. Su, S. Guo, WOₓ-surface decorated PtNi@Pt dendritic nanowires as efficient pH-Universal hydrogen evolution electrocatalysts, Adv. Energy Mater. 11 (2020) 2003192, https://doi.org/10.1002/aenm.202003192.

[34] Z. Wu, Y. Zhao, W. Xiao, Y. Fu, B. Jia, T. Ma, L. Wang, Metallic-bonded Pt-Co for atomically dispersed Pt in the Co₄N matrix as an efficient electrocatalyst for hydrogen generation, ACS Nano 16 (2022) 18038–18047, https://doi.org/10.1021/acsnano.2c04090.

[35] G. Capilli, Y. Chen, T. Szkopek, M. Cerruti, Selective catalytic electro-oxidation of water with cobalt oxide in ion impermeable reduced graphene oxide porous electrodes, ACS Nano 16 (8) (2022) 12488–12499, https://doi.org/10.1021/acsnano.2c03877.

[36] H. Jin, X. Liu, A. Vasileff, Y. Jiao, Y. Zhao, Y. Zheng, S.Z. Qiao, Single-crystal nitrogen-rich two-dimensional Mo₅N₆ nanosheets for efficient and stable seawater splitting, ACS Nano 12 (12) (2018) 12761–12769, https://doi.org/10.1021/acsnano.8b07841.

[37] C. Meng, Y. Cao, Y. Luo, Q. Kong, F. Zhang, A.A. Alshehri, K.A. Alzahrani, T. Li, Q. Liu, X. Sun, A Ni-MOF nanosheet array for efficient oxygen evolution electrocatalysis in alkaline media, Inorg. Chem. Front. 8 (2021) 3007–3011, https://doi.org/10.1039/D1QI00345C.

[38] B. Wu, S. Gong, Y. Lin, T. Li, A. Chen, M. Zhao, Q. Zhang, L. Chen, Unique NiOOH@FeOOH hetero-architecture for enhanced oxygen evolution in saline water, Adv. Mater. 26 (2022) 2108619, https://doi.org/10.1002/adma.202108619.

[39] L. Zhang, Z. Wang, J. Qiu, Energy-saving hydrogen production by seawater electrolysis coupling sulfion degradation, Adv. Mater. 21 (2022) 2109321, https://doi.org/10.1002/adma.202109321.

[40] Y. Zheng, P. Shang, F. Pei, G. Ma, Z. Ye, X. Peng, D. Li, Achieving an efficient hydrogen evolution reaction with a bicontinuous nanoporous PtNiMg alloy of ultralow noble-metal content at an ultrawide range of current densities, Chem. Eng. J. 433 (2022) 134571, https://doi.org/10.1016/j.cej.2022.134571.

[41] C. Yang, K. Dong, L. Zhang, X. He, J. Chen, S. Sun, M. Yue, H. Zhang, M. Zhang, D. Zheng, Y. Luo, B. Ying, Q. Liu, A.M. Asiri, X. Sun, Improved alkaline seawater

splitting of NiS nanosheet by iron doping, Inorg. Chem. 62 (2023) 7976–7981, https://doi.org/10.1021/acs.inorgchem.3c00836.

[42] M. Yu, J. Li, F. Liu, J. Liu, W. Xu, H. Hu, X. Chen, W. Wang, F. Cheng, Anionic formulation of electrolyte additive towards stable electrocatalytic oxygen evolution in seawater splitting, J. Energy Chem. 72 (2022) 361–369, https://doi.org/10.1016/j.jechem.2022.04.004.

[43] Y. Qiu, Z. Liu, A. Sun, X. Zhang, X. Ji, J. Liu, Electrochemical In situ self-healing of porous nanosheets based on the phase reconstruction of carbonate hydroxide to layered double hydroxides with unsaturated coordination metal sites for high-performance water oxidation, ACS Sustain. Chem. Eng. 10 (2022) 16417–16426, https://doi.org/10.1021/acssuschemeng.2c05705.

[44] H.J. Song, H. Yoon, B. Ju, D.Y. Lee, D.W. Kim, Electrocatalytic selective oxygen evolution of carbon-coated $Na_2Co_{1-x}Fe_xP_2O_7$ nanoparticles for alkaline seawater electrolysis, ACS Catal. 10 (2019) 702–709, https://doi.org/10.1021/acscatal.9b04231.

[45] J. Chang, G. Wang, Z. Yang, B. Li, Q. Wang, R. Kuliiev, N. Orlovskaya, M. Gu, Y. Du, G. Wang, Y. Yang, Dual-doping and synergism toward high-performance seawater electrolysis, Adv. Mater. 33 (2021), e2101425, https://doi.org/10.1002/adma.202101425.

[46] L. Yu, L. Wu, B. McElhenny, S. Song, D. Luo, F. Zhang, Y. Yu, S. Chen, Z. Ren, Ultrafast room-temperature synthesis of porous S-doped Ni/Fe (oxy)hydroxide electrodes for oxygen evolution catalysis in seawater splitting, Energy Environ. Sci. 13 (2020) 3439–3446, https://doi.org/10.1039/D0EE00921K.

[47] T.U. Haq, M. Pasha, Y. Tong, S.A. Mansour, Y. Haik, Au nanocluster coupling with Gd-Co_2B nanoflakes embedded in reduced TiO_2 nanosheets: Seawater electrolysis at low cell voltage with high selectivity and corrosion resistance, Appl. Catal. B Environ. 301 (2022), 120836, https://doi.org/10.1016/j.apcatb.2021.120836.

[48] J. Chen, L. Zhang, J. Li, X. He, Y. Zheng, S. Sun, X. Fang, D. Zheng, Y. Luo, Y. Wang, J. Zhang, L. Xie, Z. Cai, Y. Sun, A.A. Alshehri, Q. Kong, C. Tang, X. Sun, High-efficiency overall alkaline seawater splitting: using nickel-iron sulfide nanosheet array as a bifunctional electrocatalyst, J. Mater. Chem. A 11 (2023) 1116–1122, https://doi.org/10.1039/D2TA08568B.

[49] X. Liang, L. Wang, K. Sun, Y. Wang, Z. Xie, Q. Wu, X. Bai, M.S. Hamdy, H. Chen, X. Zou, Status and perspectives of key materials for PEM electrolyzer, Nano Res. Energy 1 (2022), e9120032, https://doi.org/10.26599/NRE.2022.9120032.

[50] X. Chen, J. Wan, J. Wang, Q. Zhang, L. Gu, L. Zheng, N. Wang, R. Yu, Atomically dispersed ruthenium on nickel hydroxide ultrathin nanoribbons for highly efficient hydrogen evolution reaction in alkaline media, Adv. Mater. 33 (2021), e2104764, https://doi.org/10.1002/adma.202104764.